Research Paper

Qualifying the design of a floating closed-containment fish farm using computational fluid dynamics

Jagan M.R. Gorle [a,*], **Bendik F. Terjesen** [a,1], **Astrid B. Holan** [a,2],
Arne Berge [b], **Steven T. Summerfelt** [c,3]

[a] Nofima AS, Sjølsengvegen 22, Sunndalsøra 6600, Norway
[b] FishGLOBE AS, Rettedalsbakkane 23, 4110 Forsand, Norway
[c] The Conservation Fund Freshwater Institute, 1098 Turner Road, Shepherdstown, WV 25443, USA

ARTICLE INFO

In order to overcome the environmental consequences of traditional net pens in producing Atlantic salmon, closed containment aquaculture systems are being developed, where the culture volume is separated from the ambient environment by an impermeable wall. However, several challenges in terms of construction and hydrodynamic properties must be solved before such systems can be used on a large scale. A study was thus performed on the design of a floating closed-containment fish farm in sea. This paper presents the design and flow analysis of two versions of the globe; first is the pilot design of a 74 m³ globe, and the second is the design of a 3500 m³ globe for post-smolts of Atlantic salmon. The results of turbulence model of the pilot globe were validated against the velocity measurements using acoustic Doppler velocimetry. Computational assessment of various flow characteristics includes the velocity and vorticity fields. The streamline pattern confirmed the secondary vortices, creating the tea-cup hydrodynamics. Coherent vortices, identified by means of Q-criterion, show the presence of vortex column in the globe. Two inlet configurations were tested on the post-smolt globe for improved performance. Design 1 has the standard one-column nozzle configuration, and the Design 2 has two-column nozzles to create a V-shaped inflow. The mixing action of the two designs was examined using Lagrangian particle tracking. Considerable influence of inlet configuration on the particle motion was observed. It was found that V-nozzles (two columns of inlet nozzles) are more effective than standard nozzles in flushing the solid particles.

* Corresponding author.
  E-mail address: gorle.jmr@gmail.com (J.M.R. Gorle).
[1] Current address: Cermaq Group AS, Dronning Eufemias gt 16, N-0102, Oslo, Norway.
[2] Current address: AquaOptima AS, Sjøgangen 4, 7010 Trondheim, Norway.
[3] Current address: Superior Fresh LLC, W15506 Superior Fresh Drive, Hixton, WI 54635 USA.

1. Introduction

The production of Atlantic salmon is the paramount activity in Norwegian aquaculture, accounting for more than 80% of the total aquaculture production in the country. With a thousand-fold growth over last four decades, Norway is currently contributing more than one third of the global salmon production. Aspiring to increase the salmon production by five times by 2050, Norwegian aquaculture has been evolving with new businesses and innovative technologies with a focus on the environmental performance of fish farms (Hagspiel, Hannevik, Lavrutich, Naustdal, & Struksnæs, 2018; Olafsen, Winther, Olsen, & Skjermo, 2012). However, there are many challenges facing this proposed five-fold expansion in production, which include sea lice, diseases, production losses etc. This necessitates innovative production systems such as closed-containment systems (CCS), where the fish are separated from the outside environment. With a better control on production, environmental impact and disease transmission makes CCS a promising alternative to open-cage production systems.

There has been a growing interest in the Norwegian aquaculture industry in CCS solutions for post-smolts (Hagspiel et al., 2018; Summerfelt, Mathisen, Holan, & Terjesen, 2016). Post-smolts are salmon being adapted to sea water life, and up to about 1 kg. Although the harvest size is about 5 kg, the post-smolt stage still amounts to approximately half the production time cycle in the sea due to the growth characteristics of salmon. By keeping the post-smolts in closed systems, this considerably reduces their exposure to sea lice, and also these systems are a more stable environment for fish production. At 4% annual growth, production in Norway should increase to 3,000,000 t by 2030. Thus, CCS plants by 2030 can be expected to account for a production of 500,000 t. The industry is therefore interested in innovative solutions to achieve this.

Little research has been done to investigate flow hydrodynamics in CCS using computational methods. However, the subject of rotational flows in confined domains has been investigated for some time, but in different applications. For instance, the early experimental studies of Willingham, Sedlak, Rossini, and Westhaver (1947), and Macleod and Matterson (1959) considered the flow behaviour in the rotary fractionation columns. Kloosterziel and van Heijst (1991) performed experiments to analyse the vortices in a rotating fluid. The study noted several observations on vortex stability, which imply that the characteristics of rotating fluid largely

depend on the type of eddies that prevail. Eddies are influenced by the type of inflow and outflow settings employed in the system. The empirical study by Dyakova and Polezhaev (2016) on the steady flow in a rotating cylinder explains the complexity associated with these flows. Furthermore, a considerable effect of the geometry of container on the flow characteristics was experimentally studied by Pieralisi, Montante, and Paglianti (2016). Although the observations made in the above literature are relevant to the present study, the experimental methods used in these investigations were enormously complex and time consuming to carry out at full-scale. On the other hand, the theoretical approach to understand the rotating flow patterns depend on far-reaching assumptions (Davoust, Achard, & Drazek, 2015; Tophoj, Mougel, Bohr, & Fabre, 2013).

Computational Fluid Dynamics (CFD) has become a promising tool to create a platform for simulation-driven product development, without the need to produce working prototypes for testing. By solving the conservation equations for mass and momentum using CFD tools, comprehensive information on various flow features can be obtained and used to improve the flow conditions.

The flow injected tangentially through a series of jets into a circular tank is inherently turbulent and several dynamic aspects associated with turbulence are experienced. Under steady inflow conditions, the rotational fluid in a closed domain experiences columnar vortical structures that align with the axis of rotational motion. Associated eddies with steep energy spectra play a major role in mixing and momentum transfer by reducing the turbulence dissipation rate that would otherwise occur (Bourouiba, Straub, & Waite, 2012; Takahashi, Ishii, & Miyazaki, 2005). The coherent vortical structures in such complex flows can be detected using various criteria. Levine, Rappel, and Cohen (2000) gives an intuitive definition of a vortex structure by presenting it as the rotational motion of several particles around a common centre. This definition can be improved by also considering the vortex convection. Vortex formation and convection is primarily accompanied by fluid shearing and thus turbulent zones (Elsas & Moriconi, 2017; Gorle, Terjesen, & Summerfelt, 2018b). Although there are several theoretical and experimental methods to determine the vortex characteristics in closed flow domains, one of the objectives of this study is to observe and compare the mixing characteristics in different geometrical designs of the closed-containment aquaculture system FishGLOBE (www.fishglobe.no).

With an increasing concern about the environmental impact of aquaculture, technologies are being developed to manage the organic waste, including the deposition of waste material as well as control of water quality due to their presence. While the near-field deposition of wastes including solids removal and stabilisation has its own challenges (Summerfelt, Adler, Glenn, & Kretschmann, 1999; Turcios & Papenbrock, 2014), the motion of solid particles in the working fluid is one of the critical aspects of operation due to its two-way interaction with the hydraulic environment; the physical and motion properties of the solids are determined by the flow field, and particle dissolution influences the water quality. In fish culture environments, solids in the water column mainly consist of faecal material and uneaten feed

pellets. Ideally, these particles should be flushed out much faster than the mean hydraulic retention time of the tank, otherwise they can adversely affect the water quality and the health and welfare of the fish. The internal fish tank geometry will also influence the flow pattern and thus the particles motion, in the context of confined flow domain. Through computational modelling, Shahrokhi, Rostami, Said, Yazdi, and Syafalni (2012) and Guo et al. (2017) identified that the efficiency of a settling tank increases with the flow uniformity. A uniform velocity field was found to increase the rate of suspended particle deposition. Active circulation zones create non-uniform conditions in the flow, which adversely affect the particle removal (Komrakova, Liu, Machado, & Kresta, 2017). Furthermore, it has been shown that Atlantic salmon growth, health and welfare is improved by increased water velocity which provides exercise training for the fish, usually in the range 1–1.5 body lengths per second (Castro et al., 2011; Gorle, Terjesen, Mota, & Summerfelt, 2018a). Therefore, any development of closed-containment systems must take this velocity requirement into account.

While reviewing the circular tank technology for aquaculture, Timmons, Summerfelt, and Vinci (1998) specified that the overall flow pattern is largely dependent on the inflow characteristics, which was experimentally proved by Muller, Cesare, and Schleiss (2017). However, quantifying studies on this topic in CCS are missing in the existing literature. This paper aims to investigate the existing design of floating, closed-containment aquaculture system-FishGLOBE, and improve the design by testing two different inlet configurations. Section 2 describes the rationale for the project, and how the design of FishGLOBE is superior to the land based farming systems. In this study, two models were investigated; a pilot globe (74 m^3 in size) and a post-smolt globe (3500 m^3 in size). While the flow field was investigated in both designs using turbulence modelling, the validation experiments were possible only for pilot globe, using Acoustic Doppler Velocimetry (ADV). In addition, the motion of biosolids in the post-smolt globe was studied using Lagrangian formulation. These investigation methods are illustrated in section 3. In section 4, a detailed information on the flow field that evolved in the pilot globe, including the effect of flow rate, is described. Based on analysis of pilot globe, which has the tangential inflow, a full-scale computational model of pilot globe was developed with two inlet configurations. Contrasting studies between both designs for flow physics and particle flushing in the post-smolt globe is presented in section 5, and conclusions made in section 6.

2.   Project FishGLOBE

FishGLOBE aims to develop a closed fish-farming facility for better fish growth and reduced production problems. The project is expected to provide a more protected environment for farming the salmon post-smolts. Combining the technology of FishGLOBE and regular open cages, it is expected to help solve some of the bigger environmental challenges, such as sea lice. The globe is equipped with diffusors, situated inside the water inlet pipes, for delivering oxygen. Furthermore, a system for CO_2 removal from reused water, based on

the use of ejectors, could be turned on if the facility experiences the difficulties with getting fresh water; thereby contributing to water quality and fish welfare during such emergencies. To achieve positive buoyancy, buoyancy tanks are located inside the upper portion of the globe, which also makes the construction stronger and resistant to the forces caused by waves. The buoyancy tanks can also be used as technical rooms, with an emergency power supply and a reserve oxygen tank. These chambers also have the equipment for filtration and handling of waste material and dead fish, as well as feed stores. The design also offers a unique solution to transport fish at high rates (>200 t h^{-1}) by creating a positive atmospheric pressure inside the structure. In addition, FishGLOBE offers most of the solutions that well boats can offer to treat the freshwater for parasites and sea lice at almost the same processing capacity. This drastically reduces the operating costs. All these operating systems are located above the rearing volume as shown in Fig. 1, where the design of the pilot globe is illustrated.

The use of closed-containment systems in aquaculture is dependent on their safe, controllable and optimal operation and systems must be tested to verify designs and confirm the desired flow pattern. Proper dimensioning and management of the hydrodynamics in the facility is imperative for water quality, fish development, health and welfare, and operating

costs. Good water quality depends on an optimal flow pattern to ensure not only better distribution of oxygen but also the efficient removal of waste products (Davidson & Summerfelt, 2004; Terjesen et al., 2013).

3. Materials and methods

3.1. Velocity measurements

A Nortek 10 MHz acoustic Doppler velocimetry (ADV) probe (Nortek AS, Vangkroken, Norway) was used in this study to measure the 3D velocity components at predefined locations within the globe. The instrument, as shown in Fig. 2, operates on the Doppler shift principle and is suitable for determining point specific velocity fluctuations but not for identifying coherent flow structures, such as the resolution of turbulent structures within a domain. ADV measurements can only be carried out within particle-laden flows (Gorle et al., 2018a). At the start of measurement, a short acoustic signal of known frequency is emitted from the transmitter. This signal is reflected in the water by the smallest particles moving with the speed of the water. The echo of the signals reflected from the measuring volume reaches the three receivers with a time shift Δt, is amplified in the signal conditioning module and
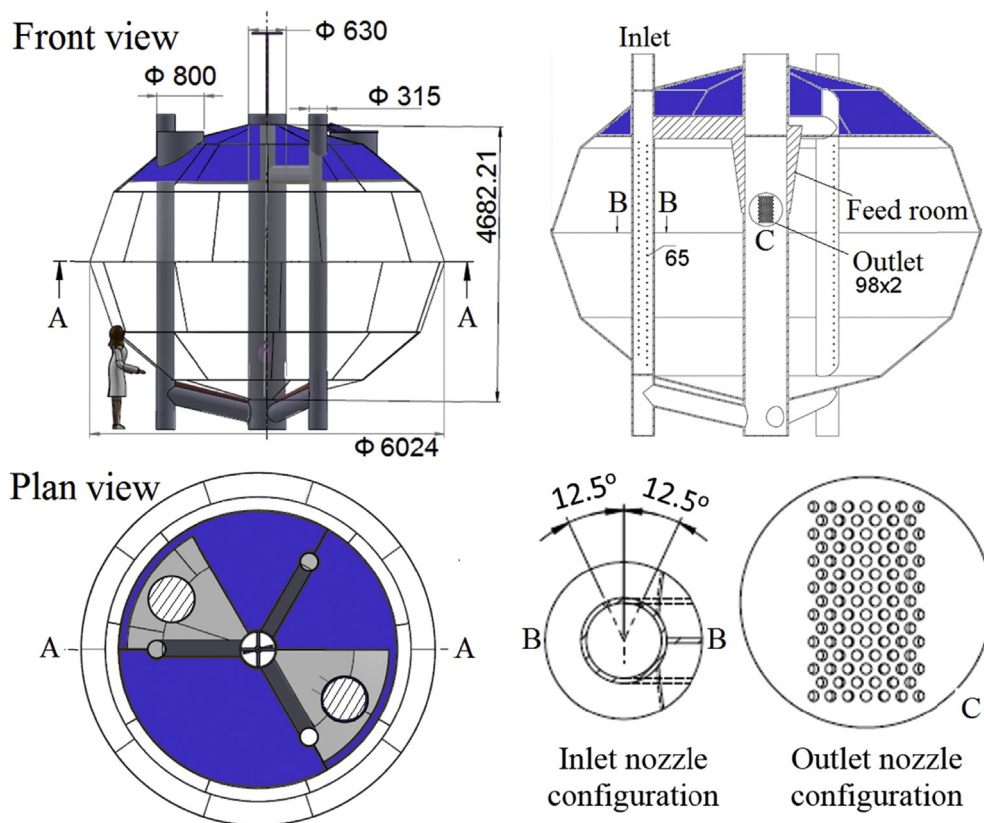
Fig. 1 – Basic design specifications of the pilot globe. Grey colour shows the space inside the globe for operating and treatment units. Two openings for velocity measurements are shown as hashed circles in the plan view. Three inlet pipes have 65 nozzles on each in two columns such that the inflow jets subtend an angle of 25° (view B–B). Water exits the globe through 98 nozzles on each side of central pipe (view C). All nozzles on inlet and outlet pipes are 20 mm diameter. (For interpretation of the references to color/colour in this figure legend, the reader is referred to the Web version of this article.)
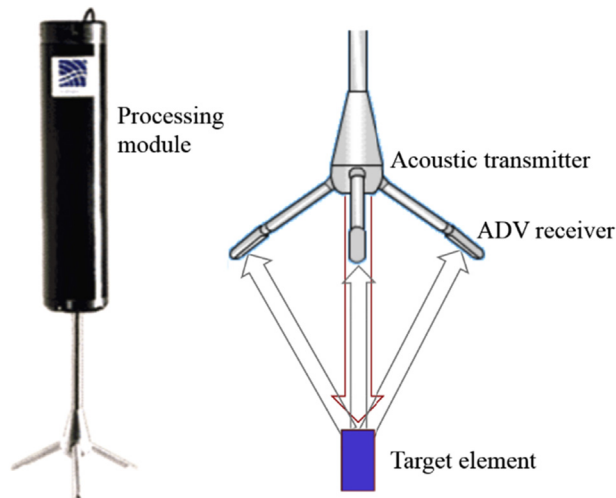
Fig. 2 – Nortek ADV probe with three receivers (left), and the process of 3D velocity measurement (right).

Fig. 3 – Correlation and SNR scores of a typical measurement. The data recording corresponds to an arbitrary location in the pilot globe with at the pump speed of 1039 rpm.

digitized and analysed in the processor. The frequency change in the acoustic signal at the time of impact on and reflection from the measuring volume caused by a relative movement of the water flowing in all three directions is proportional to the flow velocity. A stable recording for 35 kB data for each measurement, consisting of individual velocity components was collected. The momentary velocity (v), measured over a period, is temporally averaged from a turbulent fluctuating variable v'.
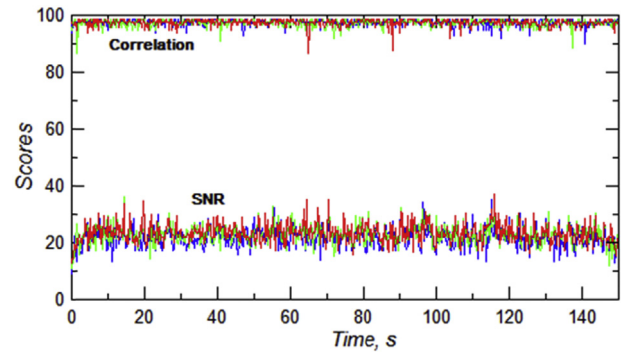
As noted by Strom and Papanicolaou (2007), the signal filtering process involves the removal of low quality data within the time series through signal correlation and signal-to-noise ratio (SNR); the former is a statistical measure of how closely the reflected pulses are related, and the latter gives the ratio between the transmitted and received signal strength. A correlation coefficient of more than 90% indicates a reliable measurement. SNR should always have values of more than 15 dB, when the data is recorded with a sampling frequency of 25 Hz. If only the mean value of the measured values is considered in the data evaluation, a SNR of 5 dB is sufficient. A typical measurement is shown in Fig. 3. However, there is a variety of parameters that lead to uncertainty in ADV measurements, particularly in turbulent flows. These include random spikes in the data, Doppler noise, too close presence of fish, and unresolved turbulent scales. Due to the lack of exclusive measurement settings for each sampling point to validate the computational predictions, a reasonable requirement is to quantify the uncertainty in velocity magnitude. This uncertainty can be reduced to some extent by fine tuning and calibration of the measurement apparatus. However, the temporal fluctuations in the flow variables necessarily produce considerable deviation from the mean values.

Referring to Fig. 4, there are two openings, each of 800 mm, on opposite sides of the globe at approximately 1.7 m from the centre, which were the only possible practical locations to measure the velocity in the globe. This limited the number of velocity measurements to 11 along three vertical lines at each operating condition.

When making field measurements, it is important to obtain reliable reference data. Due to a number of errors and uncertainties in the real-time measurements, appropriate data filtration techniques are necessary to remove wrong data sets. In the present study, a sufficiently large amount of data was collected, which reduced the degree of variation in the measurements. Figure 5 shows that the coefficient of variation (CV) at the chosen locations - lines a, b and c, is less than 1% at different pump speeds. A likely decreasing trend of CV with pump speed is observed. This means that the uncertainty associated with the equipment and measurement processes contribute more to the variations in the measurement than the uncertainty in managing an accurate flowrate into the globe.

3.2. Computational methodology

3.2.1. Workflow
In the context of complex geometries used here, a reliable multi-physics analysis and a cost-effective workflow were required. Figure 6 shows the schematic workflow, used in this work.

The transfer of CAD data from one computational engine to the other is a challenging task, particularly in the case of complex geometries. Older data formats such as STL and IGES/IGS offer a surface representation based CAD data transfer, which is not suitable for exchanging the product data structures and solid model definitions. On the other hand, the formats STEP/STP can efficiently transfer such metadata and provides a standard interoperability of data exchange between different computer programs. The software package CATIA V5 R21 (Dassault Systèmes, Vélizy-Villacoublay, France) was used to develop the geometry models in STEP/STP format. To create a control volume domain, an automated meshing process using Castnet (DHCAE Tools GmbH, Germany) was implemented. However, the meshing interface was limited only to the imports of Parasolid or STL models. Therefore, an efficient CAD translation from STP to X_T was
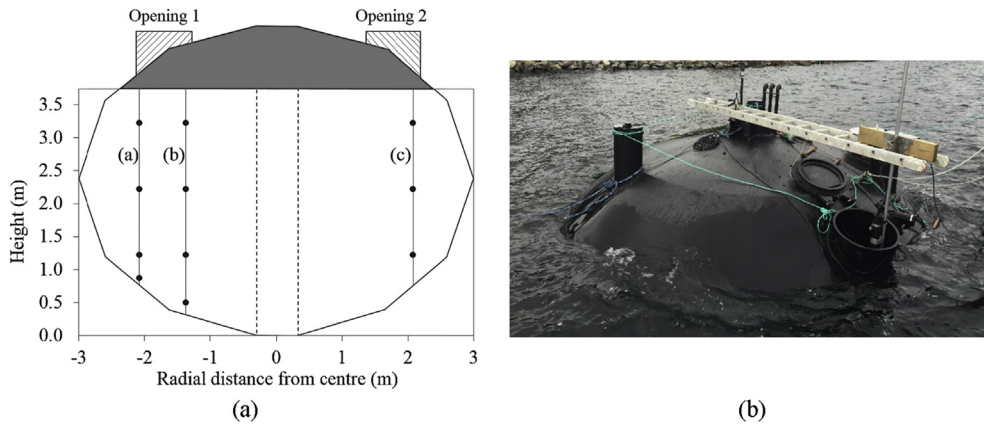
Fig. 4 − **Process of velocity measurements. (a) Distribution of measurement points along three vertical lines - a, b and c. Flow from the inlet first reaches the measurement line 'c'. (b) Vector measuring instrument, deployed at the site.**
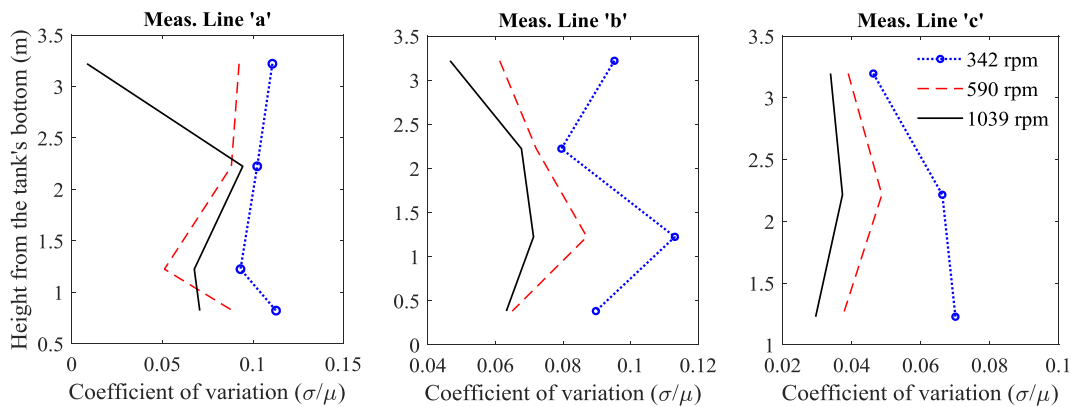
Fig. 5 − **Coefficient of variation (CV) along the measurement lines a, b and c, to assess the data reliability. Less than 1% of CV at all operating conditions imply sufficiently large amount of data and efficient removal of spikes.**

performed using the conversion software, 3D-Tool V12 (3D-Tool GmbH & Co. KG, Weinheim, Germany).

A finite volume based CFD tool that works with OpenFOAM technology, called BlueCFD (BlueCAPE, Casais da Serra, Portugal), was used for simulations. While offering a wide range of viscous and multiphysics solvers, BlueCFD-Core 2.3, in association with a graphical interface, called RunGui, constituted the simulation environment for the present study. The results comprised both field representations and quantified parameters, which were post-processed using Paraview 5 (Kitware, New York, USA) and Matlab R17 (MathWorks, Natick, Massachusetts, USA).
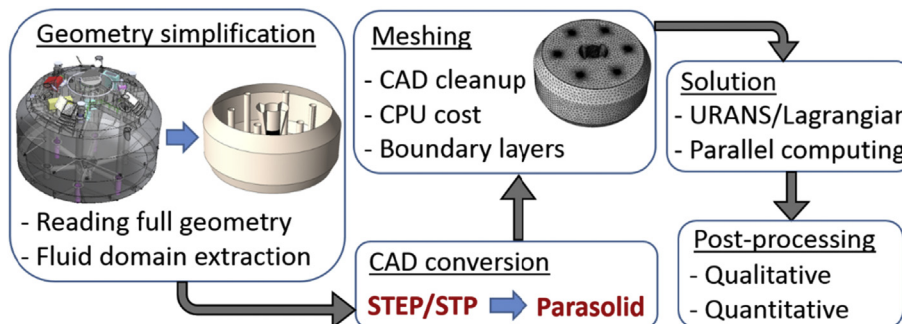
Fig. 6 − **Workflow design, from geometry development to post-processing.**

3.2.2. Turbulence modelling

The dimensions and geometry of the globe ensure the flow domain is inherently turbulent, which requires turbulence modelling. To describe the fluid dynamics in the globe, the mass and momentum conservation equations were selected in transient conditions, which are:

$$\nabla \cdot (\overline{v}) = 0$$

$$\frac{\partial}{\partial t}(\overline{v}) + \nabla \cdot (\overline{v} \otimes \overline{v}) = -\frac{1}{\rho}(\nabla \overline{p} - \nabla \cdot (\tau + R))$$

where τ is the stress-tensor, expressed in mean velocity, and $R = -\overline{v' \otimes v'}$ is called the Reynolds stress tensor, which represents the turbulence. Boussinesq approach is used to model the turbulence, where Reynolds stress tensor is expressed in terms of turbulent viscosity μ_t as:

$$R = \frac{\mu_t}{\rho}(\nabla \overline{v} + (\tau)\nabla \overline{v}) - \frac{2}{3}k\delta$$

Turbulent kinetic energy is defined by $k = 0.5\,\overline{v'^2}$, which is related to the velocity fluctuations. The role of the turbulence modelling is to model the eddy viscosity μ_t. The Spalart-Allmaras model is not sufficient to do this due to its inability to compute the flow shear and anisotropic turbulence. Out of the widely used two-equation models, the Realisable $k - \varepsilon$ model exhibits superior performance in capturing the streamline curvature, rotation, recirculation and round jets, which makes it suitable for the present study (Adamčík, Svěrák, & Peciarc, 2017; Gorle et al., 2018b). The model is so formulated that the normal Reynolds stresses are positive and shear Reynolds stresses satisfy Schwarz inequality (Shih, Liou, Shabbir, Yang, & Zhu, 1995). Also, it has the improved capability of resolving the boundary layers under adverse pressure gradients and flow separation through two-layer approach. To determine the turbulent viscosity, Realisable $k - \varepsilon$ turbulence model solves the transport equations for turbulent kinetic energy k and its dissipation rate ε, which are

$$\frac{\partial}{\partial t}(k) + \frac{\partial}{\partial x_j}(kv_j) = \frac{1}{\rho}\frac{\partial}{\partial x_j}\left[\left(\mu + \frac{\mu_t}{\sigma_k}\right)\frac{\partial k}{\partial x_j}\right] + P_k - \varepsilon$$

$$\frac{\partial}{\partial t}(\varepsilon) + \frac{\partial}{\partial x_j}(\varepsilon v_j) = \frac{1}{\rho}\frac{\partial}{\partial x_j}\left[\left(\mu + \frac{\mu_t}{\sigma_\varepsilon}\right)\frac{\partial \varepsilon}{\partial x_j}\right] + C_1\varepsilon\sqrt{2S_{ij}S_{ij}} - \frac{C_2\varepsilon^2}{k + \sqrt{\nu\varepsilon}}$$
$$+ C_{1\varepsilon}\frac{\varepsilon}{k}P_k$$

where P_k is the generation of turbulent kinetic energy k. C_1 is computed from $\max\left[0.43, \frac{k\sqrt{2S_{ij}S_{ij}}}{k\sqrt{2S_{ij}S_{ij}}+5\varepsilon}\right]$. $C_2 = 1.9$ and $C_{1\varepsilon} = 1.44$ are the model constants. Turbulent viscosity is calculated from

$$\mu_t = \rho C_\mu \frac{k^2}{\varepsilon}$$

where

$$C_\mu = \frac{\varepsilon}{4.04\varepsilon + A_S k\sqrt{6\left(S^2 + \Omega^2\right)}\cos\varphi}$$

and

$$\varphi = \frac{1}{3}\cos^{-1}\left(\sqrt{6}\,\frac{S_{ij}S_{ji}S_{ki}}{\sqrt{S_{ij}S_{ji}}}\right)$$

The inclusion of tensor $S^2 + \Omega^2$ in computing C_μ plays an important role in predicting the rotational and deformation components of the flow field, which is an advantage over other two-equation models.

3.2.3. Lagrangian particle tracking

In addition to hydrodynamic characteristics of the rearing facility, it is important to ensure if the design promotes self-cleaning of feed and faecal particles released by the fish in the globe. In this study, the passive transport of solid particles in the globe was investigated using a Lagrangian approach. Under given operating conditions, samples of particles are injected in a predefined fashion, which follow the motion equations

$$\frac{dx}{dt} = v_p$$

$$m\frac{dv_p}{dt} = f$$

where v_p is the velocity of the particle of mass m, which experiences a force of f. The momentum equation of the particle as noted by Elghobashi (1994) is

$$f = \underbrace{-\frac{\pi d^2}{8}\rho C_D|v_p - v|(v_p - v)}_{Drag} + \underbrace{mg}_{Gravity} - \underbrace{\rho g\vartheta}_{Buoyancy}$$

where d is the particle diameter, C_D is the particle's drag coefficient, ϑ is the particle volume and v is the instantaneous flow velocity, modelled using Reynolds decomposition. A *random-walk* algorithm was used to couple the deterministic variables with the stochastic ones (Bechtold, Vanderborght, Ippisch, & Vereecken, 2011), where the particle trajectory is formulated within the uncorrelated eddies. The interaction time of the particles was determined from the minimum of integral time scale of turbulence in the Lagrangian frame (T_L), and the time the particles spent in traversing the eddy (T_p). The following equations were used to determine these characteristics.

$$T_L = \frac{k}{\varepsilon}$$

$$T_p = C_p\frac{k^{3/2}}{\varepsilon|v_p - v - v'|}$$

where C_p is the model constant (=0.164). The trajectory of the particle was calculated by updating turbulence parameters and thus the characteristic times at every time step. This eddy interaction model (EIM) assumes isotropic turbulence ($v_1^2 = v_2^2 = v_3^2$), which leads to over-predictions of wall-normal velocity components in the boundary layer. Therefore, a DNS-based correction factor was introduced in the stochastic model in the vicinity of the solid walls ($y^+ < 80$) in order to account for the anisotropy in the turbulence. The

local fluctuating velocity components were therefore computed from

$$v_i' = g_i N_i \sqrt{\frac{2k}{3}}$$

where N_i is a random number generated from Gaussian probability distribution and the function g_i in the Cartesian coordinates is computed from

$$g_1 = 1 + 0.285 (y^+ + 6) \exp\left[-0.455 (y^+ + 6)^{0.53} \right];$$

$$g_2 = 1 - \exp\left[-0.02 y^+ \right]$$

$$g_3 = \sqrt{3 - g_1^2 - g_2^2}$$

The non-dimensional wall-distance is defined by $y^+ = v^* y / \nu$, where y is the cell normal distance from the wall, ν is the kinematic viscosity of the fluid. The frictional velocity v^* is the function of wall shear stress.

3.2.4. Parallel computation

In the context of increasing demands for high fidelity computational studies in designing and analysing flow systems, powerful computing machines, with a rapid technological evolution in their architecture, have been in use for about 30 years. Multicore processors with highly capable shared memory nodes have become the fulcrum of advanced computations. The development of an efficient computational model is not a straightforward process and it requires many different skills. The physics of the flow were first modelled using a robust numerical framework, followed by the implementation of solution process on parallel computing machine. Parallel processing involves the domain decomposition, where the computational grid and its associated fields are partitioned to be handled by separate processors. OpenFOAM employs process-level parallelism between the processors using the standard, message passing interface (MPI), which levers the communication between different tasks through data exchange (Fig. 7).

The parallel processing of MPI protocol in the present study used the Scotch heterogeneous decomposition, which requires no geometric information and thus reduces the number of patches between the processors (Chevalier & Pellegrini,

2008). Because the amount of data communication is reduced, the performance could be increased. Figure 8 shows the resulting 26 subdomains after decomposing the computational grid.

4. Pilot globe (volume of 74 m³)

4.1. Pre-processing

For the computational modelling of the hydrodynamics in the pilot globe of 74 m³ volume, a simple CAD model was developed by eliminating all internal supporting structures and operating systems inside the globe. The resulting geometry was discretised into finite volumes to solve the conservation equations. The fundamental aspects that distinguish computational grids are cell shape and size, which determine the solution accuracy. A widely-accepted fact is that the hexahedral cells yield better accuracy than the tetrahedral cells (Benzley, Perry, Merkley, Clark, & Sjaardema, 1995; Shepherd & Johnson, 2008). However, a critical review of computational meshes is particularly important for industrial applications where the geometries are often complex, and a trade-off between the ease of mesh generation and solution accuracy is necessary. The computational study of Hosseini, Patel, Ein-Mozaffari, and Mehrvar (2010) on the multiphase modelling of an agitated tank used tetrahedral cells to create the unstructured mesh over complex surfaces. However, being the lowest order polyhedral construction, the tetrahedral cells occupy the space less efficiently for a given resolution, and thus demand more memory and high CPU time. Concerning the boundary layers, where the viscous effects lead the momentum transport, Ito and Nakahashi (2004) acknowledged that the hexahedral meshes are more effective in predicting the flow gradients than the tetra meshes. Kowalski, Ledoux, and Frey (2012) noted that the complicated domains could be covered by a full hexahedral mesh by ensuring the good quality in terms of cell dihedral angle and Jacobian measure. In order to benefit from the full hexahedral cells, the meshing process was considered to generate a dominantly structured hexahedral mesh.

Although the transient turbulent simulations require sufficiently fine resolution in the node spacing, minimising the
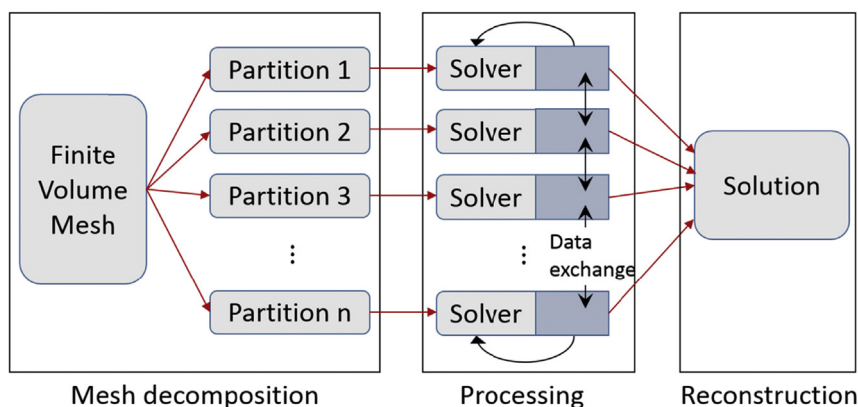
Fig. 7 − Process of parallel computation.

180° 135° 90° 45° 0° 45° 90° 135° 180°
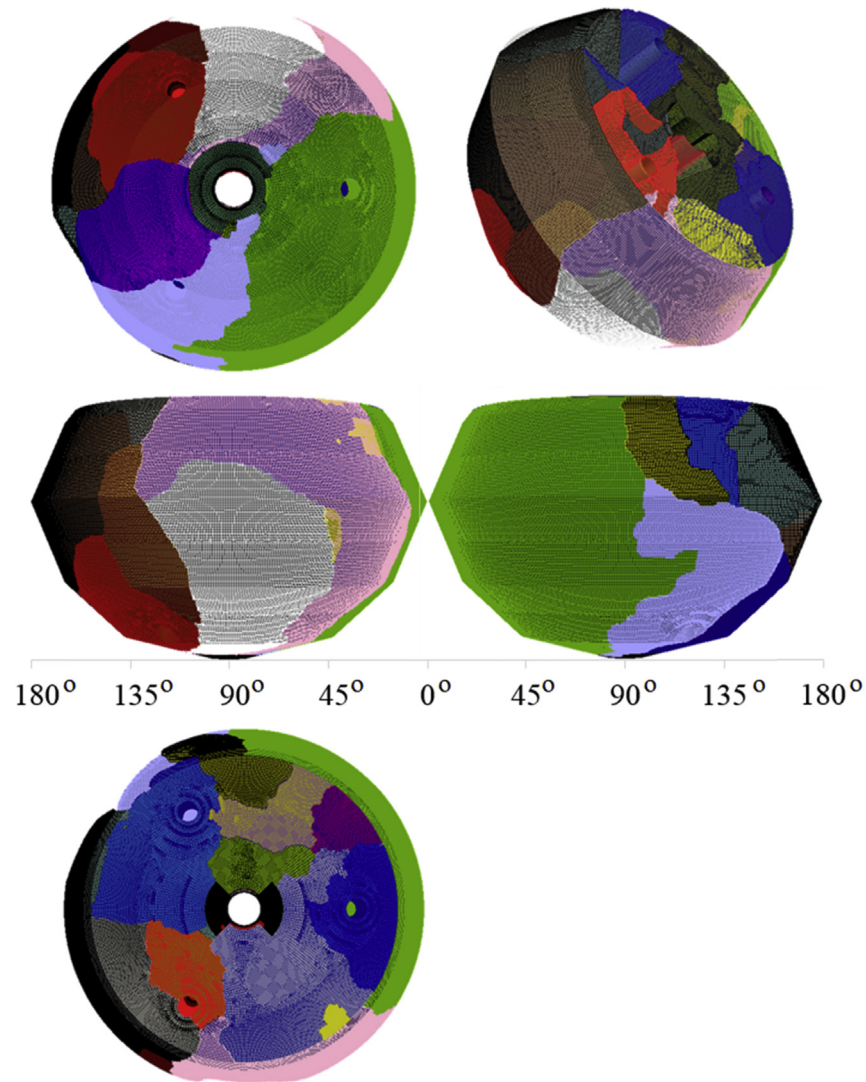
Fig. 8 – Domain decomposition into 26 partitions of the FishGLOBE, presented in a 3rd angle view.

number of cells has a huge payback in terms of computational cost. Several mesh dependence studies were conducted by changing the base cell size until the velocity magnitude in the regions of high gradients (near inlet and outlet) did not change by more than 2%. As a result, a hexa mesh with 484,112 cells was developed (Fig. 9). Because the mesh quality significantly affects the solution accuracy by influencing the discretisation error (Diskin & Thomas, 2012), different mesh quality

Fig. 9 – (a) Mesh visualization on external surface, and (b) internal surface of the FishGLOBE. The mesh is predominantly structured with hexahedral cells.

parameters were examined. 98% of mesh cells had the aspect ratio less than 10, and 99% had the dihedral angle between 70° and 130°. 92% of cells had the skewness less than 0.8 with 55% less than 0.5. This confirmed good quality of discretized domain.

4.2.   Problem setup

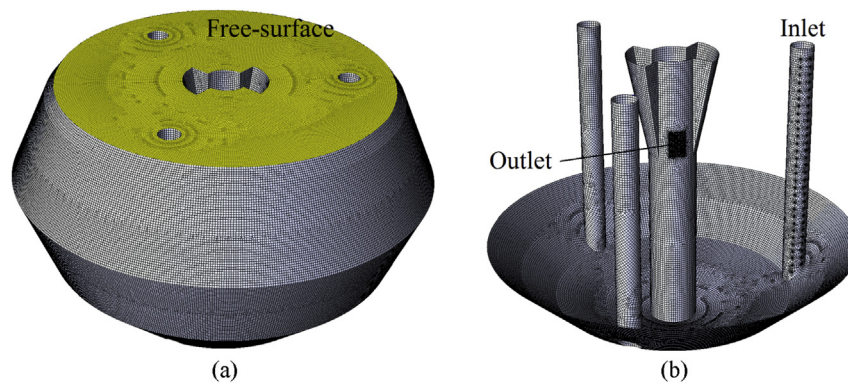The working fluid was water. The computations were performed by defining the inlet nozzles with a volume flow rate specification. In case of the pilot globe, the four pump speeds − 342 rpm, 590 rpm, 1039 rpm and 1350 rpm correspond to the mass flow rates of 300 l min^{-1}, 736 l min^{-1}, 1344 l min^{-1} and 1672 l min^{-1}, respectively. In addition, the turbulence intensity $\left(\iota = \frac{v'}{v}\right)$ and turbulence length scale $\left(\ell = C_\mu \frac{k^{3/2}}{\varepsilon}\right)$ were required to define the inlet boundary conditions. Because the flow was discharged through the inlet pipe of 0.315 m diameter to the inlet consisting of 65 nozzles of 20 mm size each, the turbulence intensity and length scale at the inlet were considered to be in the order of 1%. However, different inlet turbulence conditions were tested (up to 6%) and no significant changes in the solution were observed. These parameters are, however, not available in the standard output of the $k - \varepsilon$ model because the fluctuating velocity component cannot be computed by the model. Instead, turbulent kinetic energy was considered for the flow evaluation. The exit nozzles on the central pipe were given pressure outlet condition. The walls of the globe were assigned no-slip boundary conditions with zero roughness. The free surface in the case of confined flow domains is often modelled using Volume of Fluid technique (Yang & Zhou, 2015; Peric & Abdel-Maksoud, 2016). Such sophisticated multiphase models often suffer from solver instability and high computational cost. The dynamics of free surface is not covered in the scope of the current study. Rather, we applied a shear free surface boundary condition (Luan, Zhang, Wei, & Duan, 2017; Peaudecerfa et al., 2017) ignoring the shape of and perturbations on free surface.

The simulations were initiated with a first-order upwind discretisation in space and time until the solution was converged, and then switched to second-order accuracy. The pressure and velocity fields were coupled using the SIMPLE (semi-implicit method for pressure linked equations) algorithm with second order interpolation. The transient formulation contains the time step 0.005 s with 30 sub-iterations. The residuals of computed flow variables were set to the order of 10^{-3} as convergence criteria, and no further change in the solution was observed with further reduction in the target residual value. The computations were started at low under-relaxation factors, which were raised to default values after a stable solution was witnessed. A 14-core Intel Xeon E5-2683 v3 2.00 GHz workstation with 28 processors was employed for the computations.

4.3.   Model validation

Before analysing the flow field in the globe, the developed computational model was validated against the velocity measurements at predefined locations under different operating conditions. Figure 10 compares the CFD predictions of
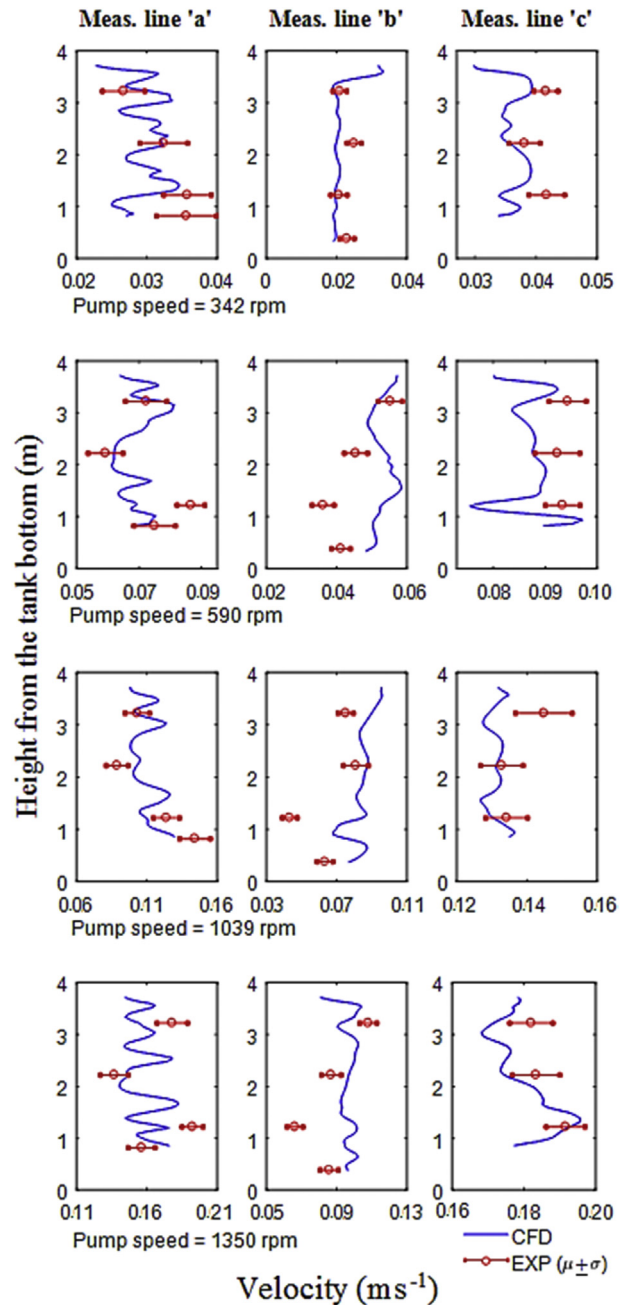
Fig. 10 − Velocity profiles along the measurement lines a, b and c at different pumping conditions. Higher velocities are registered along the line 'c' as it is close to inlet pipe. Line 'a' is on the same radial position as line 'c', which has recorded slightly lower velocities than line 'a' due to momentum diffusivity. EXP indicate data points of actual velocity measurements, mean ± standard deviation.

velocity magnitude along the lines (a), (b) and (c) from the ADV measurements. The standard deviation bars that accompany the experimental results, quantify the uncertainty in the measurements. This variation in the velocity does not necessarily represent the uncertainty in the measurement utilities alone, but it includes the flow rate through inlet pipes as well. Because the error in the flow rate into the globe is

unknown, the analysis is therefore limited only to the magnitude of deviation but not its source.

Although a close match between the experimental and computational results is evident, a little under-prediction along the line 'b' and over-prediction along the line 'c' by CFD are observed. Particularly at higher flow rates, the computational results deviate from the measurements along the line 'b'. Although the Realisable $k - \varepsilon$ model is known to perform better than the other two-equation models in capturing the swirling and rotating flow motion, the model's efficiency in accurately predicting the small-scale flow patterns in a closed flow domain is still debatable (Diaz & Hinz, 2015).

The spatial variation of velocity along the line 'c' is due to the jets from each flow inlet nozzle. In addition, the interactions between the local flow and near boundaries such as free surface, conical wall surface and bottom of the globe are not homogeneous. Irregularity in the velocity profile is preserved along the flow path as seen along the line 'a'. On the other hand, the velocity magnitude and its scale of variation are comparatively lesser along the line 'b'. This shows that strong velocity gradients exist in the radial direction. Also, a reduction in the velocity magnitude is observed as the flow travels from the location 'c' to 'a', which explains the momentum diffusivity in space. The flow velocity on free surface displays a different behaviour along the radius. The free surface velocity is higher than at depth along the line 'b', which is possibly due to flow suction by the outlet on the central vertical pipe. But, at extremely high flow rates, the stress-free wall surface boundary condition caused underestimated velocity predictions by CFD. Fluctuations in divergence of the free surface velocity field is associated with a range of turbulence scales. Better accuracy could be ensured using a two-phase flow model at the free surface but this would produce a small gain in accuracy and cost more in terms of CPU time.

4.4. Flow field analysis

The conical bottom for fish tanks plays an important role in self-cleaning of the tank. FishGLOBE adopted this concept to create the secondary vortices in the flow by keeping the primary rotational flow free from perturbations and non-uniform flow structures. It is therefore interesting to investigate the effect of Reynolds number (Re) on the characteristics of secondary vortices in a confined flow domain. Figure 11 (a) − (d) show the streamline distribution across the central vertical plane at different operating conditions. For comparison purposes, the contour plot is coloured on the scale of a normalised velocity. Referring to Fig. 11 (a), region 1 is characterised by high velocity and hence strong shear stresses, which is likely to be narrowed down at higher pumping conditions. This is due to the increasing normalised velocity in the vicinity of region 1, implying more uniform flow in the tank. There is an increased vortex formation in the region 2 with pump speed, but this is at the expense of losing vortices in region 3. In addition, there is a new vortex growing in region 4 at high flow rates. Increasing flow velocity deforms the vortex combo at the location 5, which tends to move to the bottom of the tank. The vortex position and strength in region 6 is also influenced by the pump speed, but limited by the confined flow domain. It is observed that the flow structure along the vertical line through region 7 is little impacted by the increased flowrate due to equally dominant rotational flow near the tank's periphery and radial flow from the core to the centre of the globe. However, investigating the relationship between these two flow components is out of the scope of present study. By and large, the obtuse-angled corners of the globe control the velocity field for any flowrate. It is thus concluded that the design of pilot globe maintains effective 'tea-cup hydrodynamics' to promote mixing and self-cleaning of the tank (Gorle et al., 2018b).

The vortices are characterised by the peaks of low pressure. However, Jeong and Hussain (1995) noted that the minimum local pressure is not a sufficient condition, though necessary, to identify the vortices. This led to the definition of the tensor $S^2 + \Omega,^2$ where $S_{ij} = 0.5\,(v_{i,j} + v_{j,i})$ and $\Omega_{ij} = 0.5\,(v_{i,j} - v_{j,i})$ are the symmetric and antisymmetric components of velocity gradient. The Q criterion, as computed by Gorle, Chatellier, Pons, and Ba (2016) identified the vortices as the regions, where the flow is dominated by the rotation tensor.
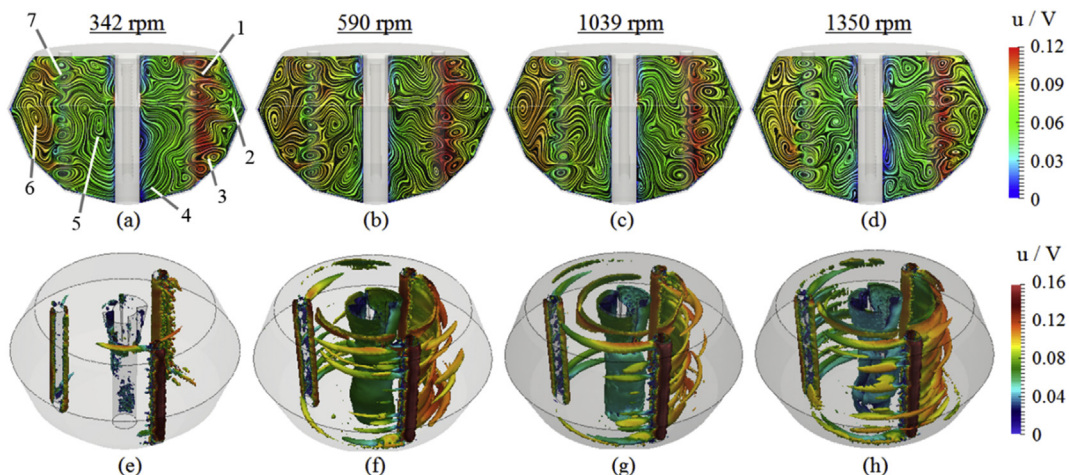

Fig. 11 − **Flow visualisation in the pilot globe at different inlet pump operating parameters (a)−(d) show the streamline pattern across the central vertical plane. (e) and (f) show vorticity distribution using Q = 0.005, and (g) and (h) using Q = 0.02.**
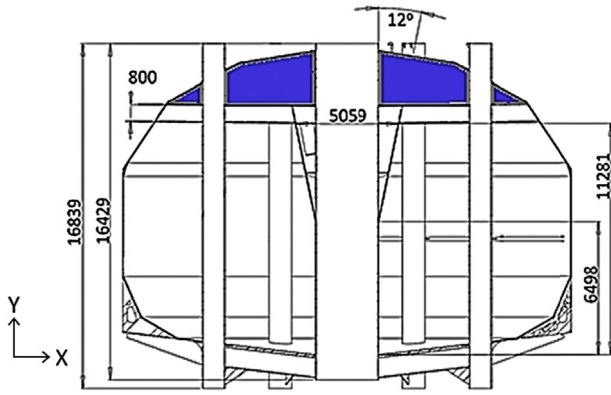
Fig. 12 − Basic dimensions of post-smolt globe (volume of 3500 m³). Blue colour represents the space for operating equipment. All dimensions are in mm. (For interpretation of the references to color/colour in this figure legend, the reader is referred to the Web version of this article.)

Mathematically, it is defined as $Q = 0.5 (\Omega_{ij}\Omega_{ij} - S_{ij}S_{ij})$. Consequently, the vortex structures are identified by a representation of the positive Q iso-values, while their centres are identified by the maximum values of Q. The evolution of vortices at different pump speeds are visualised in Fig. 11(e)−(h) using iso Q-value. The intensity of circulation increases with flow rates. Two major regions of vortices are observed in all cases. One is the vortex ring around the central outlet pipe, and the other is envelope of vorticity that covers the inlet pipes. On a general note, these two regions comprise turbulent energy cascade processes. The individual vortical structures advected away from the inlet pipes in Fig. 11(f) and (g) along the outer envelope have merged to form a continuous columnar vortex in the globe at higher flow rates as shown in Fig. 11(h). The wake zones behind the inlet pipes can be stretched by the vortex core followed by a gradual entrainment into the envelope. Enriched flow dynamics in this region are often difficult to accurately model. Stripping, stretching and wrapping of vortices generate a wide range of turbulence scales (Kawahara, Kida, Tanaka, & Yanase, 1997), which challenge the ability of available turbulence models to capture the pertinent physics.
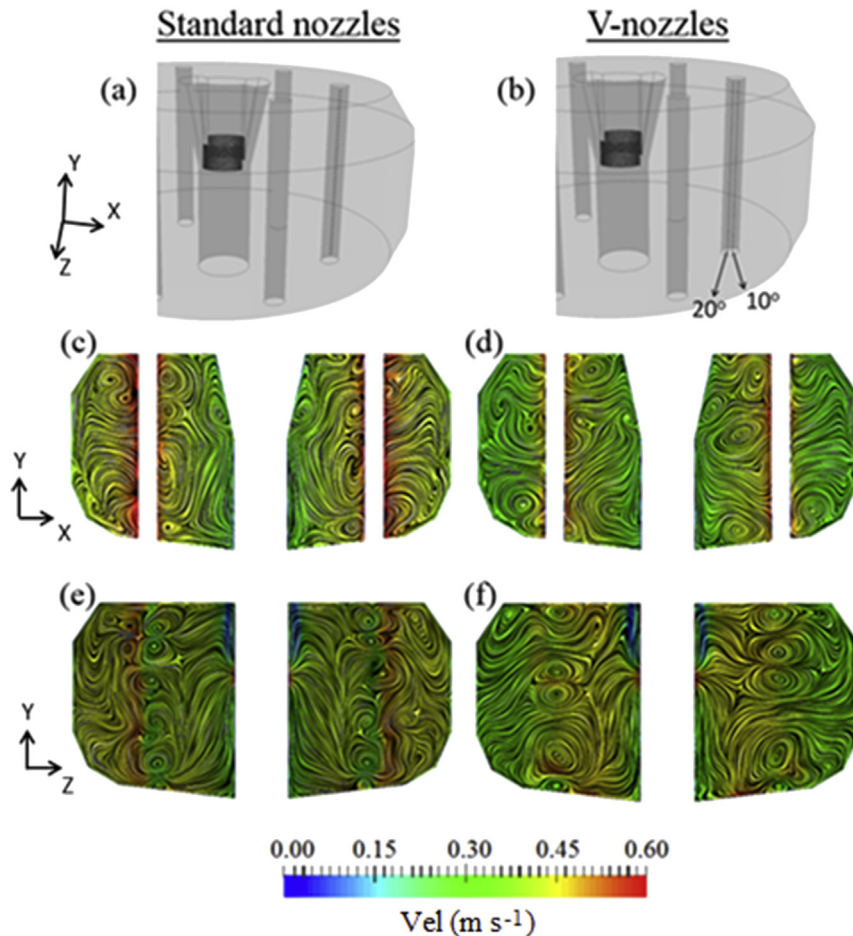
Fig. 13 − Design of standard and V-nozzles. (a) 40 standard nozzles, each of 125 mm diameter deliver the water into the globe tangential to the wall. (b) 160 nozzles with 6.3 cm diameter each, placed in two columns with 80 in each. The inner column of the nozzles deliver the water at 20° angle towards the centre of the globe, and the outer nozzle supplies water at 10° away from the centre. Resulting streamline pattern on XY plane for (c) standard, and (d) V-nozzles. The same distribution on ZY plane are shown in (e) for standard nozzles, and in (f) for V-nozzles.

5.   Post-smolt globe (volume of 3500 m³)

5.1.   Geometry

In order to exploit the advantages of CCS as seen in the case of pilot globe, a post-smolt facility with an expected production of 250 t of salmon in a rearing volume of 3500 m³ is in the development phase. The design of the post-smolt globe was computationally tested to determine if the design produces the optimal flow conditions and mixing in the globe. Figure 12 shows the geometry and basic dimensions of the post-smolt globe. In addition to increasing the water volume by ~50 times from the size of the pilot globe, there are two major changes in the geometries of the two designs. Firstly, the conical part wall of the pilot globe that has the largest radius was replaced by the straight vertical wall. This would expect to result in a change in the development of vortices in the region 2 as in Fig. 11(a). Secondly, the number of inlet pipes was increased from 3 to 6. However, the computational model was developed with only two inlet pipes operating to supply a total flow of 1.98 m³ s⁻¹.

From several possible configurations for the nozzles on the inlet pipes in terms of their size, shape and orientation, two nozzle designs were considered and compared for their performance. The first design has a standard series of 40 nozzles,

each having the diameter of 125 mm, placed along the height of each inlet pipe. The nozzles are tangential to the wall of the globe and so is the inflow direction. In the second design, the flow is discharged through 160 nozzles, divided into two columns such that a V-type inflow feature is created. The inner column directs the flow at an angle of 20° towards the centre of the globe, while the outer column of nozzles discharges the flow at 10° away from the tangent. The nozzle size in this case is 63 mm. Figure 13(a) and (b) show the respective nozzle designs that confirm an equal inlet velocity of 2 m s⁻¹, when 0.99 m³ s⁻¹ flow is discharged through each inlet pipe into the globe.

5.2.   Flow field analysis

The streamline patterns across the two vertical planes, XY and ZY in the globe with the proposed nozzles are illustrated in Figs. 13(c)–(f). The flow is accelerated around solid obstructions such as inlet pipes. Flow from the standard nozzles, which is purely tangential to the walls, follows a pure circular path in the globe. This feature displays a higher velocity around the obstruction, than that in case of V-nozzles. In addition, standard nozzle design creates a concentrated velocity distribution along the radial position of inlet pipes, which is more distributed across the plane in case of V-nozzle design. Both designs display the presence of secondary
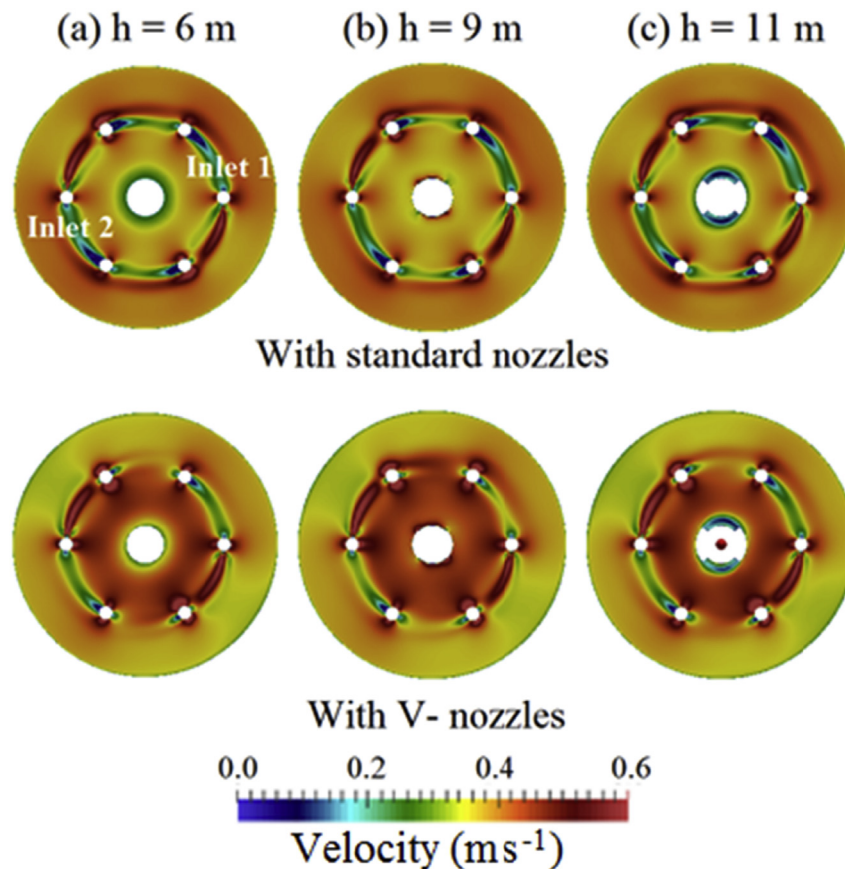

Fig. 14 – Planar distribution of velocity magnitude at different heights in the post-smolt globe with standard nozzles and V-nozzles. Higher velocities are recorded near the periphery with the standard nozzles (top), and in the core with the V-nozzles (bottom).

Table 1 – Uniformity index γ at different planar locations in the post-smolt globe with standard and V-nozzle inlet designs.

Location	Standard nozzles	V-nozzles
h = 6 m	0.938	0.937
h = 9 m	0.930	0.904
h = 11 m	0.930	0.929

vortices along the vertical planes, which retain the 'tea-cup' effect and promote mixing activity.

The rotational velocity across the globe was analysed using the velocity distribution across the horizontal plane. Figure 14 distinguishes both nozzles for planar velocity distributions at different heights from the base of the globe. All planar visuals display a common trait; a maximum velocity from the two inlet pipes and the major flow gradients along the ring of inlet pipes. This qualitative locus separates the velocity field; standard nozzles create higher velocities outside this ring and a lower velocity inside. V-nozzles on the other hand create higher velocities inside the ring than the outside. Comparing the wake region downstream of the inlet pipes, the inner series of nozzles deliver the flow with a radial component, and therefore a lesser tendency to interact with the pipe on downstream. This leads to a reduced wake area behind the pipes, which implies a reduced form drag. The wake area in case of standard nozzles is comparatively larger, and

relatively more energy should be spent overcoming the drag force induced by low-pressure wake.

One of the major concerns in aquaculture hydrodynamics is the flow uniformity, which is a critical parameter for a uniform distribution of dissolved oxygen across the domain. Otherwise, dead zones can develop, with sub-optimal water quality and the potential for reduced self-cleaning of feed and faecal matter. Flow analysis on the horizontal planes in Fig. 14 was therefore extended to compute the flow uniformity index γ. Since the flow uniformity is a function of Re, which in turn is a function of turbulence intensity, it is interesting to distinguish the designs in terms of γ, which is defined as

$$\gamma = 1 - \int_A \frac{\sqrt{(\bar{v} - v)^2}}{2A\bar{v}} dA$$

Table 1 shows the γ indices across the horizontal planes at different heights for the two designs. Both designs have appreciable difference in the velocity distribution. With the standard nozzles, the peak velocities are gradually reduced from the periphery to the centre. In contrast, V-nozzles caused the velocity to jump suddenly from the lower values in the periphery to higher values in the core. This resulted in somewhat lower uniformity indices for the globe with V-nozzles, compared to standard nozzles. However, as observed by Gorle et al. (2018b), this difference is of no practical effect because the overall uniformity was never below 90% in both cases.

(a) Standard nozzles   (b) V-nozzles

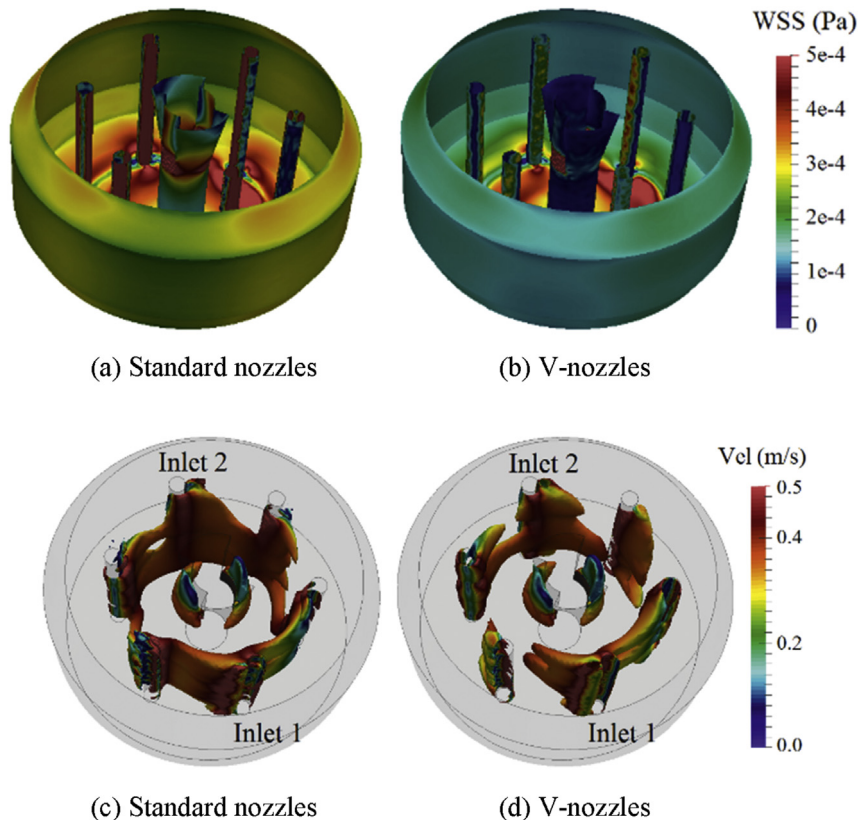(c) Standard nozzles   (d) V-nozzles

Fig. 15 – Distribution of wall shear stress in the post-smolt globe with (a) standard nozzles, and (b) V-nozzles iso-contours of turbulent kinetic energy, coloured on velocity scale for (c) standard nozzle design, and (d) V-nozzle design.

The velocity fields in Fig. 14 raises a concern about the energy loss from the flow to the solid surfaces. Wall shear stress (WSS) was used to quantify the energy loss in both the designs, which is defined as

$$\tau_w = (\mu_d + \mu_t)\frac{dv}{dy}$$

where μ_d and μ_t are the molecular and turbulent viscosities, respectively. Thus, WSS estimates the turbulent friction on the walls. In an incompressible flow field, the flow friction on the walls is purely dependent on the wall roughness and viscous effects of the flow. Figure 15 (a) and (b) demonstrate a clear contrast between the two designs in terms of the WSS distribution. Pure tangential flow leads to more intensive collision on the walls of the globe, and hence more energy is deposited in the wall and not in the flow of water. Inclusion of a radial component in flow through V-nozzles decreased the WSS, and hence the energy loss by approximately 40%.

Another advantage of V-nozzles is that the jets emanating from 2 columns of nozzles into the upstream flow tend to organize themselves with the mean flow quickly. This controls the wake size behind the inlet pipes, which is not the case with standard nozzles. Wake consists of shear zones and characterized by severe turbulence. The knowledge of the fine structures of turbulence in the flow domain can help identify the critical regions, where flow field fluctuations are maximum. This is important because turbulence intervenes in the phenomena of flow uniformity, mixing and particle settling. Turbulent structures apparently appear downstream of each inlet pipe with the peaks near the inlet nozzles. The transport mechanisms increase in these regions due to the prevailing transient characteristics of eddies, which extract the kinetic energy from the mean flow. Figure 15 (c) and (d) depict the 3D contours of turbulent kinetic energy k in the globe of selected inflow designs with an iso-value of 0.007. It is clear that the standard nozzles create stronger velocity gradients than V-nozzles, which result in increased production of turbulent kinetic energy. The turbulent kinetic energy dissipates more quickly in the case V-nozzles. Negligible turbulent kinetic energy distribution was observed in both cases near the tank walls compared to the peaks of distribution.

5.3. Particle motion

Although the volume fraction of solids in the globe is very small compared to the size of the globe, the particles adversely impact the water quality and hence the welfare and performance of the fish (Cripps & Bergheim, 2000; Thorarensen & Farrell, 2011). Uneaten feed pellets and fish faeces, if left in the culture tank, are hydrolysed or decomposed by micro-organisms which reduces the dissolved oxygen in the water and increases CO_2, NH_3 and other mineral nutrients. Thus, the uneaten feed particles should be removed from the tank to prevent these wastes from further degrading into fine particulates and dissolved organic matter that exerts an oxygen demand, ammonia, and dissolved phosphorous, as well as to control the eutrophication and potentially hypoxic conditions in the receiving water. The solids in the flow domain should be treated to meet the quality standards. To facilitate an effective self-cleaning action, optimised flow conditions and structural

design is necessary. A separate particle trapping system exists in the post-smolt globe, which along with the particles discharges 1% of the flow. A further investigation was carried out to measure the effectiveness of solids flushing in both the standard and V-nozzle designs. In the first step, the working fluid was characterized as the water-solids mixture. The liquid phase is defined by its density, viscosity, average velocity, while the solid phase is characterized by particle size, shape, density and particle cohesion, which determine the rate of sedimentation in the globe. When the particle size is relatively small with respect to the flow dimension, turbulence plays a major role in the flow of the water/solids mixture.
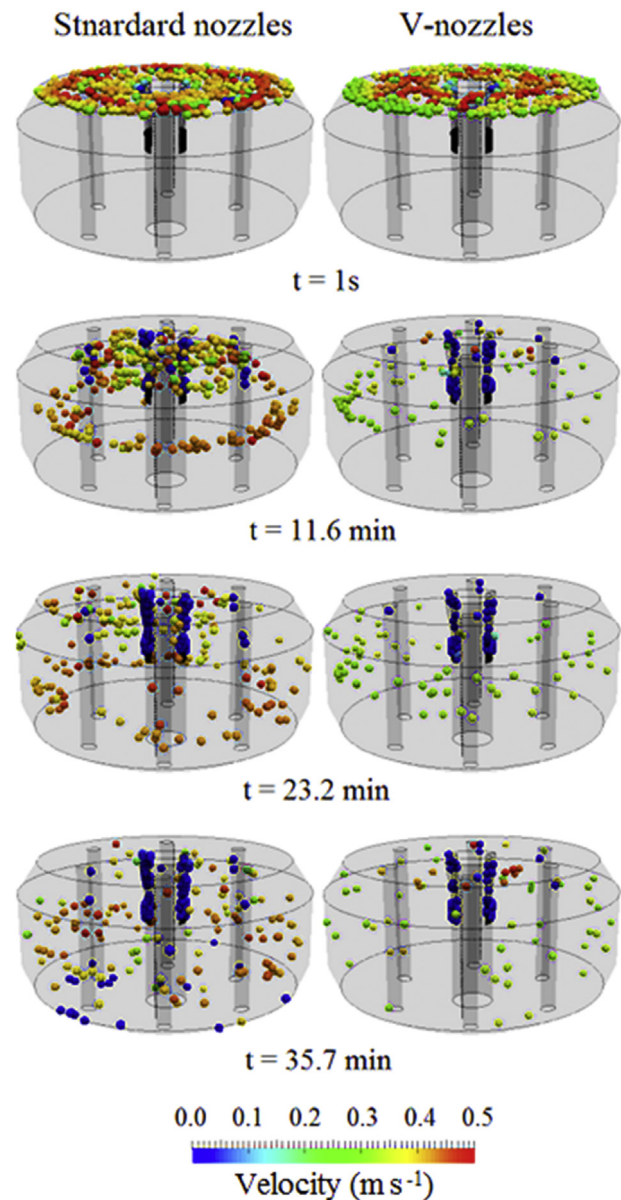

Fig. 16 – **Faecal particle dispersion in post-smolt globe with standard and V-nozzle designs at different times after particle injection at free surface. Particle size is up-scaled by ×750 for visualisation purposes.**

In order to evaluate the particle motion in the selected designs, two types of particles, fish faeces and feed pellets, were used to investigate the motion of the solids in the globe. The density of fish faecal matter is likely to vary depending upon operating conditions. Suspended solid specific gravity values of 1.13–1.20 and 1.005 were reported by Timmons and Young (1991), and Robertson (1992), respectively. The study of Unger and Brinker (2013) on a variety of fish diets indicated a mean specific gravity of 1.036 ± 0.0018 of faecal matter from 0.3 to 0.4 kg sized rainbow trout. Also, the settling velocity of the particles varies with the size of the particles. These authors found that the settling velocity increases with particle size from 1 mm s^{-1} for 200 μm faecal particles to 6–9 mm s^{-1} for 600 μm size. These wide variations likely reveal the diversity of such complex hydrodynamic systems. In the present study, fish faecal particles with a mass-averaged diameter of 200 μm and a specific gravity of 1.036 were modelled as they were injected through the water surface at an initial settling velocity of 4 mm s^{-1}.

Galileo number (Ga) determines the influence of flow on the particle settling, which is the ratio of buoyancy to viscous force. The physical properties of the feed pellets vary with fish species and size in aquaculture, and were determined from a theoretical consideration. The diameter of the feed pellets may vary between 1 and 10 mm with the highest density of 1150 kg m^{-3}, which corresponds to a maximum Galileo number of 1000. The mean residence time of the particles was determined by the non-dimensional parameter called the Stokes number, which is defined by

$$Stk = \frac{\rho_p d^2 \mathbf{v}}{18 \mu_d L}$$

where ρ_p and d are the density and size of the particle, $\mathbf{v}$ is flow velocity, L is the characteristic length, which is the maximum diameter of the globe in the present case. When $Stk \ll 1$, the particle follows the flow, whereas $Stk \gg 1$ represents a weak influence of the flow on the particle's motion. At a flow rate of 0.99 m^3 s^{-1} from each of two operating inlet pipes, the Stokes numbers of the faeces and feed pellets are negligibly small a two-way coupling between the motions of flow and particles

is not necessary. The solids in this study were thus assumed to have the suspended motion. In such intrinsic suspension transport, the particles will seldom be in contact with the bottom of the globe, but always carried away by the flow.

In order to track the particles through the longest travelling distance, the particles were injected at the water surface. For the sake of simple analysis, the number of particles injected was limited to 500 in a fully developed Eulerian flow field. It was also assumed that there were no collisions among the particles. A standard wall interaction with a coefficient of 0.5 for the particles was used in the solution process. Figure 16 shows the resulting distribution of particles in the globe for the selected inlet configurations at different times after the particle have been injected. As soon as the particles enter the flow domain, the particles attained the characteristics of the flow, as explained in Fig. 14. Higher peripheral velocity with the standard nozzles moves the particles in this region with higher momentum, which happens near the centre with V-nozzles. Particle settling occurs along the flow length under the influence of kinetic energy of the flow, gravity force and evacuation through the outlet holes. The snapshots at $t = 11.6$ min show that the particles in V-nozzle design move swiftly towards the outlet and get discharged out of the tank, resulting in a fewer particles left. The stronger central vortex forming in the standard nozzle design is likely to prevent the particles to go close to the outlet. At $t = 23.2$ min, higher particle momentum continues near the periphery of the tank in the case of standard nozzles. This reveals that the loss of uniformity with V-nozzles as explained in section 5.2 has become an advantage because fewer particles are near the periphery of the tank, since they are difficult to move towards the central outlet. Furthermore, the solids removal efficiency of both inlet configurations was compared for particle residence time. Figure 17 shows the percentage of particles removed as the particles were injected at time $t = 0$. Standard nozzle design takes approximately 45 min to steadily flush 40% of particles. V-nozzle design moves more than half of the particles in less than 17 min, which results in a steeper profile. This corresponds to the self-cleaning effectiveness of V-nozzles is approximately two times higher than that standard
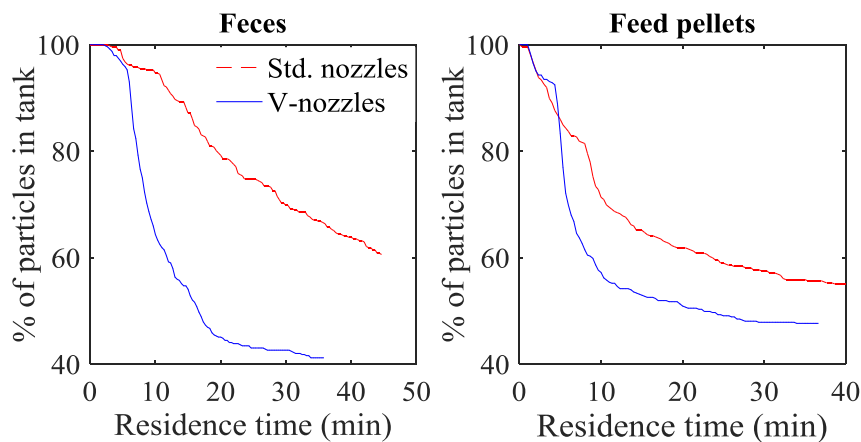

Fig. 17 – Comparison between the two nozzle designs for residence time distribution of faecal particles (left) and feed pellets (right) in the post-smolt globe.

nozzle design. In case of feed pellets, both nozzle designs displayed identical trends, although V-nozzles took 65% less time than the standard nozzles to flush 40% of particles.

6. Conclusions

This paper presents the development of CFD models of a closed-containment aquaculture system. Such aquaculture systems are increasingly being focused on as a technology that can lead to further growth of the salmon farming industry (e.g. Calabrese et al., 2017; Summerfelt et al., 2016). There is a lack of scientific information for the development of innovative solutions in the field of hydrodynamics in aquaculture systems. Using CFD, this study has developed new inlet designs to improve the flow patterns. The following three aspects are worth noting.

Measurements and modelling: ADV was used for velocity measurements in the pilot globe at 11 predefined locations. Although the amount of information obtained from the experiments was enough to validate the computational model, the measurements are not sufficient to fully understand the turbulence features in the globe. However, it is possible to estimate the variance and covariance of velocity components using ADV, which can improve the quality of flow characterisation. Despite the assumptions made in relation to the instrument geometry, acoustic device efficiency and the target element positioning, Voulgaris and Trowbridge (1998) recorded a deviation of only 1% in the mean velocity and Reynolds stresses using ADV from true values. The deviation was 5%, when the turbulent boundary layer flows over a smooth bed was studied by Dombroski and Crimaldi (2007). Future studies should empirically study the levels of turbulence in the globe.

Flow characterisation: This study demonstrated the effect of inflow rate on the flow domain of a closed-containment aquaculture system. It was found that this flow field is characterized by enriched vortex dynamics, associated with the vortex column and rings. The conical corners of the pilot globe largely control the presence of secondary vortices. With the information obtained from the CFD studies of the pilot globe, a much larger post-smolt globe was simulated with two different inlet configurations under the hypothesis that inlet configuration has a major impact on the flow domain. It was discovered that V-nozzle configuration for the inlet pipes displayed a superior performance to the standard nozzles in terms of vorticity distribution and energy preservation, and was only penalised by a 2% reduction in mean uniformity of the flow. Other nozzle configurations that can improve the flow pattern are possible and this requires further study. In addition, the positioning of inlet and outlet pipes could be a fruitful area for future research.

Particles in the flow: The motion dynamics of faeces and uneaten feed pellets were well-captured in this study. The inlet configuration was found to have substantial influence on the particle distribution in the globe and their settling features. V-nozzles displayed approximately three times better performance in flushing the solids than the standard nozzles. The simple particle-tracking model used in the present study did not consider the collisions. This could be addressed in the future using a stochastic collision formulation (Pischke, Kneer,

& Schmidt, 2015) which requires appropriate information on the mechanical properties of the solids concerned. This is more challenging and yet untouched research topic in the field of aquaculture and it requires multi-particle dynamics modelling of combinations of feed and faeces at high *Re*.

The next step in the project FishGLOBE is to develop a grow-out globe to farm bigger fish, sized 100 g–3 kg. The expected rearing volume would be 29,000 m^3, capable of holding 2300 t of fish. Such large constructions, with enormous amounts of flow transferring to and from the globe, would necessarily create high Reynolds effects with complex flow dynamics. Future computational studies on this grow-out globe will consider the outcomes of the present study to create favourable flows and operating conditions.

REFERENCES

Adamčík, M., Svěrák, T., & Peciarc, P. (2017). Parameters effecting forced vortex formation in blade passageway of dynamic air classifier. *Acta Polytechnica, 57*(5), 304–315. https://doi.org/10.14311/AP.2017.57.0304.

Bechtold, M., Vanderborght, J., Ippisch, O., & Vereecken, H. (2011). Efficient random walk particle tracking algorithm for advective-dispersive transport in media with discontinuous dispersion coefficients and water contents. *Water Resources Research, 47*(10), W10526. https://doi.org/10.1029/2010WR010267.

Benzley, S. E., Perry, E., Merkley, K., Clark, B., & Sjaardema, G. (1995). A comparison of all hexagonal and all tetrahedral finite element meshes for elastic and elasto-plastic analysis. In *Proceedings of 4th international meshing roundtable* (Vol. 17, pp. 179–191). Albuquerque, New Mexico, USA. October 16-17.

Bourouiba, L., Straub, D. N., & Waite, M. L. (2012). Non-local energy transfers in rotating turbulence at intermediate Rossby number. *Journal of Fluid Mechanics, 690*, 129–147. https://doi.org/10.1017/jfm.2011.387.

Calabrese, S., Nilsen, T. O., Kolarevic, J., Ebbesson, L. O. E., Pedrosa, C., Fivelstad, S., et al. (2017). Stocking density limits for post-smolt Atlantic salmon (Salmo salar L.) emphasis on production performance and welfare. *Aquaculture, 468*, 363–370. https://doi.org/10.1016/j.aquaculture.2016.10.041.

Castro, V., Grisdale-Helland, B., Helland, S. J., Kristensen, T., Jørgensen, S. M., Helgerud, J., et al. (2011). Aerobic training stimulates growth and promotes disease resistance in Atlantic salmon (Salmo salar). *Comparative Biochemistry and Physiology Part A: Physiology, 160*(A), 278–290. https://doi.org/10.1016/j.cbpa.2011.06.013.

Chevalier, C., & Pellegrini, F. (2008). PT-Scotch: A tool for efficient parallel graph ordering. *Parallel Computing, 34*(6–8), 318–331. https://doi.org/10.1016/j.parco.2007.12.001.

Cripps, S. J., & Bergheim, A. (2000). Solids management and removal for intensive land-based aquaculture production systems. *Aquacultural Engineering, 22*, 33–56. https://doi.org/10.1016/S0144-8609(00)00031-5.

Davidson, J. T., & Summerfelt, S. T. (2004). Solids flushing, mixing, and water velocity profiles within large (10 and 150 m³) circular 'Cornell-type' dual-drain tanks. *Aquacultural Engineering, 32*(1), 245–271. https://doi.org/10.1016/j.aquaeng.2004.03.009.

Davoust, L., Achard, J. L., & Drazek, L. (2015). Low-to-moderate Reynolds number swirling flow in an annular channel with a rotating end wall. *Physical Review E, 91*(2). https://doi.org/10.1103/PhysRevE.91.023019, 023019.

Diaz, D. D. O., & Hinz, D. F. (2015). *Performance of eddy-viscosity turbulence models for predicting swirling pipe-flow: Simulations and laser-doppler velocimetry.* arXiv:1507.04648 [physics.flu-dyn].

Diskin, B., & Thomas, J. (2012). Effects of mesh regularity on accuracy of finite-volume schemes. In *50th AIAA aerospace sciences meeting (AIAA 2012-0609)*. USA: Nashville, Tennessee. https://doi.org/10.2514/6.2012-609. January 9-12.

Dombroski, D. E., & Crimaldi, J. P. (2007). The accuracy of acoustic Doppler velocimetry measurements in turbulent boundary layer flows over a smooth bed. *Limnology and Oceanography: Methods, 5*(1), 23–33. https://doi.org/10.4319/lom.2007.5.23.

Dyakova, V., & Polezhaev, D. (2016). Oscillatory and steady flows in the annular fluid layer inside a rotating cylinder. *Shock and Vibration, 7162368*, 1–8. https://doi.org/10.1155/2016/7162368.

Elghobashi, S. (1994). On predicting particle-laden turbulent flows. *Applied Scientific Research, 52*(4), 309–329. https://doi.org/10.1007/BF00936835.

Elsas, J. H., & Moriconi, L. (2017). Vortex identification from local properties of the vorticity field. *Physics of Fluids, 29*(1). https://doi.org/10.1063/1.4973243, 015101.

Gorle, J. M. R., Chatellier, L., Pons, F., & Ba, M. (2016). Flow and performance analysis of H-Darrieus hydroturbine in a confined flow: A computational and experimental study. *Journal of Fluids and Structures, 66*, 382–402. https://doi.org/10.1016/j.jfluidstructs.2016.08.003.

Gorle, J. M. R., Terjesen, B. F., Mota, V. C., & Summerfelt, S. T. (2018a). Water velocity in commercial RAS culture tanks for Atlantic salmon smolt production. *Aquacultural Engineering, 81*, 89–100. https://doi.org/10.1016/j.aquaeng.2018.03.001.

Gorle, J. M. R., Terjesen, B. F., & Summerfelt, S. T. (2018b). Hydrodynamics of octagonal culture tanks with Cornell-type dual-drain system. *Computers and Electronics in Agriculture, 151*, 354–364. https://doi.org/10.1016/j.compag.2018.06.012.

Guo, H., Ki, S. J., Oh, S., Kim, Y. M., Wang, S., & Kim, J. H. (2017). Numerical simulation of separation process for enhancing fine particle removal in tertiary sedimentation tank mounting adjustable baffle. *Chemical Engineering Science, 158*, 21–29. https://doi.org/10.1016/j.ces.2016.09.022.

Hagspiel, V., Hannevik, J., Lavrutich, M., Naustdal, M., & Struksnæs, H. (2018). Real options under technological uncertainty: A case study of investment in a post-smolt facility in Norway. *Marine Policy, 88*, 158–166. https://doi.org/10.1016/j.marpol.2017.11.020.

Hosseini, S., Patel, D., Ein-Mozaffari, F., & Mehrvar, M. (2010). Study of solid-liquid mixing in agitated tanks through computational fluid dynamics modelling. *Industrial & Engineering Chemistry Research, 49*, 4426–4435. https://doi.org/10.1021/ie901130z.

Ito, Y., & Nakahashi, K. (2004). Improvements in the reliability and quality of unstructured hybrid mesh generation. *International Journal for Numerical Methods in Fluids, 45*(1), 79–108. https://doi.org/10.1002/fld.669.

Jeong, J., & Hussain, F. (1995). On identification of a vortex. *Journal of Fluid Mechanics, 285*, 69–94. https://doi.org/10.1017/S0022112095000462.

Kawahara, G., Kida, S., Tanaka, M., & Yanase, S. (1997). Wrap, tilt and stretch of vortex lines around a strong thin straight vortex tube in a simple shear flow. *Journal of Fluid Mechanics, 353*, 115–162. https://doi.org/10.1017/S0022112097007246.

Kloosterziel, R. C., & van Heijst, G. J. F. (1991). An experimental study of unstable barotropic vortices in a rotating fluid. *Journal of Fluid Mechanics, 223*, 1–24. https://doi.org/10.1017/S0022112091001301.

Komrakova, A. E., Liu, Z., Machado, M. B., & Kresta, S. M. (2017). Development of a zone flow model for the confined impeller stirred tank (CIST) based on mean velocity and turbulence measurements. *Chemical Engineering Research and Design, 125*, 511–522. https://doi.org/10.1016/j.cherd.2017.07.025.

Kowalski, N., Ledoux, F., & Frey, P. (2012). A PDE based approach to multidomain partitioning and quadrilateral meshing. In *Proceedings of the 21st international meshing roundtable* (pp. 137–154). https://doi.org/10.1007/978-3-642-33573-0_9. San Jose, California, USA.

Levine, H., Rappel, W. J., & Cohen, I. (2000). Self-organization in systems of self-propelled particles. *Physical Review E, 63*. https://doi.org/10.1103/PhysRevE.63.017101, 017101.

Luan, D., Zhang, S., Wei, X., & Duan, Z. (2017). Effect of the 6PBT stirrer eccentricity and off-bottom clearance on mixing of pseudoplastic fluid in a stirred tank. *Results in Physics, 7*, 1079–1085. https://doi.org/10.1016/j.rinp.2017.02.034.

Macleod, N., & Matterson, K. J. (1959). The performance of rotary concentric cylinder fractionating columns -1. *Chemical Engineering Science, 10*(4), 254–267. https://doi.org/10.1016/0009-2509(59)80060-9.

Muller, M., Cesare, G. D., & Schleiss, A. J. (2017). Experiments on the effect of inflow and outflow sequences on suspended sediment exchange rates. *International Journal of Sediment Research, 32*, 155–170. https://doi.org/10.1016/j.ijsrc.2017.02.001.

Olafsen, T., Winther, U., Olsen, Y., & Skjermo, J. (2012). *Value creation from productive oceans in 2050. Report from a working group establish by DKNVS and NTVA.* Trondheim, Norway.

Peaudecerf, F. J., Landel, J. R., Goldstein, R. E., & Luzzatto-Fegiz, P. (2017). Traces of surfactants can severely limit the drag reduction of superhydrophobic surfaces. *Proceedings of the National Academy of Sciences, 114*(28), 7254–7259. https://doi.org/10.1073/pnas.1702469114.

Peric, R., & Abdel-Maksoud, M. (2016). Reliable damping of free surface waves in numerical simulations. *Ship Technology Research, 63*(1), 1–13. https://doi.org/10.1080/09377255.2015.1119921.

Pieralisi, I., Montante, G., & Paglianti, A. (2016). Prediction of fluid dynamic instabilities of low liquid height-to-tank diameter ratio stirred tanks. *Chemical Engineering Journal, 295*, 336–346. https://doi.org/10.1016/j.cej.2016.03.026.

Pischke, P., Kneer, R., & Schmidt, D. P. (2015). A comparative validation of concepts for collision algorithms for stochastic particle tracking. *Computers & Fluids, 113*, 77–86. https://doi.org/10.1016/j.compfluid.2015.01.018.

Robertson, W. D. (1992). *Assessment of filtration and sedimentation systems for total phosphorus removal at the lake utopia fish culture station. Canadian fish culture operations.* Blacks Harbour, (New Brunswick, Canada: Aquaculture Division, Connors Bros. Limited.

Shahrokhi, M., Rostami, F., Said, M. A. M., Yazdi, S. R. S., & Syafalni, S. (2012). The effect of number of baffles on the improvement efficiency of primary sedimentation tanks. *Applied Mathematical Modelling, 36*(8), 3725–3735. https://doi.org/10.1016/j.apm.2011.11.001.

Shepherd, J. F., & Johnson, C. R. (2008). Hexahedral mesh generation constraints. *Engineering with Computers, 24*(3), 195–213. https://doi.org/10.1007/s00366-008-0091-4.

Shih, T. S., Liou, W. W., Shabbir, A., Yang, Z., & Zhu, J. (1995). A New k-ε eddy viscosity model for high Reynolds number

turbulent flows. *Computers & Fluids, 24*(3), 227–238. https://doi.org/10.1016/0045-7930(94)00032-T.

Strom, K. B., & Papanicolaou, A. N. (2007). ADV Measurements around a cluster microform in a shallow mountain stream. *Journal of Hydraulic Engineering, 133*(12), 1379–1389. https://doi.org/10.1061/(ASCE)0733-9429(2007)133:12(1379).

Summerfelt, S. T., Adler, P. R., Glenn, D. M., & Kretschmann, R. N. (1999). Aquaculture sludge removal and stabilization within created wetlands. *Aquacultural Engineering, 19*(2), 81–92. https://doi.org/10.1016/S0144-8609(98)00042-9.

Summerfelt, S. T., Mathisen, F., Holan, A. B., & Terjesen, B. F. (2016). Survey of large circular and octagonal tanks operated at Norwegian commercial smolt and post-smolt sites. *Aquacultural Engineering, 74*, 105–110. https://doi.org/10.1016/j.aquaeng.2016.07.004.

Takahashi, N., Ishii, H., & Miyazaki, T. (2005). The influence of turbulence on a columnar vortex. *Physics of Fluids, 17*(3). https://doi.org/10.1063/1.1858532, 035105.

Terjesen, B. F., Summerfelt, S. T., Nerland, S., Ulgenes, Y., Fjæra, S. O., Reiten, B. K. M., et al. (2013). Design, dimensioning, and performance of a research facility for studies on the requirements of fish in RAS environments. *Aquacultural Engineering, 54*, 49–63. https://doi.org/10.1016/j.aquaeng.2012.11.002.

Thorarensen, H., & Farrell, A. (2011). The biological requirements for post-smolt Atlantic salmon in closed-containment systems. *Aquaculture, 312*, 1–14. https://doi.org/10.1016/j.aquaculture.2010.11.043.

Timmons, M. B., Summerfelt, S. T., & Vinci, B. J. (1998). Review of circular tank technology and management. *Aquacultural Engineering, 18*(1), 51–69. https://doi.org/10.1016/S0144-8609(98)00023-5.

Timmons, M. B., & Young, W. D. (1991). Considerations on the design of raceways. In P. Giovannini (Ed.), *Proceedings of world aquaculture society and American society of agricultural engineers (ASAE publication 02–91). San JuanAquaculture systems engineering*. St. Joseph, MI, USA: PR American Society of Agricultural Engineers. June 16-20.

Tophoj, L., Mougel, J., Bohr, T., & Fabre, D. (2013). Rotating polygon instability of a swirling free surface flow. *Physical Review Letters, 110*, 1–5. https://doi.org/10.1103/PhysRevLett.110.194502.

Turcios, A. E., & Papenbrock, J. (2014). Sustainable treatment of aquaculture effluents - what can we learn from the past for the future? *Sustainability, 6*, 836–856. https://doi.org/10.3390/su6020836.

Unger, J., & Brinker, A. (2013). Feed and treat: What to expect from commercial diets. *Aquacultural Engineering, 53*, 19–29. https://doi.org/10.1016/j.aquaeng.2012.11.012.

Voulgaris, G., & Trowbridge, J. H. (1998). Evaluation of the Acoustic Doppler Velocimeter (ADV) for turbulence measurements. *Journal of Atmospheric and Oceanic Technology, 15*, 272–289. https://doi.org/10.1175/1520-0426(1998)015<0272:EOTADV>2.0.CO;2.

Willingham, C. B., Sedlak, V. A., Rossini, F. D., & Westhaver, J. W. (1947). Rotary concentric-tube distilling column. *Industrial Engineering & Chemistry, 39*(6), 706–712. https://doi.org/10.1021/ie50450a004.

Yang, F. L., & Zhou, S. J. (2015). Free surface turbulent flow in an unbaffled stirred tank: Detached eddy simulation and VOF Study. *Chemical and Biochemical Engineering Quarterly, 29*(3), 395–403. https://doi.org/10.15255/CABEQ.2014.2056.